Comparison between 3-D-PTV and 2-D-PIV for determination of hydrodynamics of complex fluids in a stirred vessel

Alberini, F.; Liu, Li; Stitt, E.h.; Simmons, Mark

DOI:
10.1016/j.ces.2017.05.034

Document Version
Publisher's PDF, also known as Version of record

Citation for published version (Harvard):
Alberini, F, Liu, L, Stitt, EH & Simmons, M 2017, 'Comparison between 3-D-PTV and 2-D-PIV for determination of hydrodynamics of complex fluids in a stirred vessel', *Chemical Engineering Science*, vol. 171, pp. 189–203. https://doi.org/10.1016/j.ces.2017.05.034

Chemical Engineering Science 171 (2017) 189–203

Contents lists available at ScienceDirect

Chemical Engineering Science

journal homepage: www.elsevier.com/locate/ces

Comparison between 3-D-PTV and 2-D-PIV for determination of hydrodynamics of complex fluids in a stirred vessel

F. Alberini [a,*], L. Liu [b], E.H. Stitt [b], M.J.H. Simmons [a]

[a] School of Chemical Engineering, University of Birmingham, B15 2TT, UK
[b] Johnson Matthey Technology Centre, Billingham TS23 1LB, UK

HIGHLIGHTS

- Applicability of 3D-PTV for the blending of Newtonian and non-Newtonian fluids.
- The measurements compared against 2D-PIV data.
- Experiments in the laminar (Re ~ 70), transitional (Re ~ 1000) and turbulent.
- Data in terms of average flow field and fluctuating components.
- Comparisons between the Eulerian PIV data and the Euler-Lagrangian PTV data.

ARTICLE INFO

Article history:
Received 30 January 2017
Received in revised form 16 May 2017
Accepted 19 May 2017
Available online 22 May 2017

Keywords:
3-D-PTV
2-D-PIV
Transitional regime
Turbulent regime
Non-Newtonian fluids

ABSTRACT

The capabilities of 3-D-Particle Tracking Velocimetry (PTV) to measure flow fields during the blending of Newtonian and non-Newtonian fluids in a standard baffled cylindrical vessel are assessed. The results are benchmarked against conventional 2-D Particle Image Velocimetry (PIV) data. The vessel, of diameter T = 0.19 m, is equipped with a 6-blade down-pumping PBT impeller of diameter, D = 0.5T. Experiments in the low transitional (Re ~ 70), and transitional (Re ~ 1000) regimes have been conducted, using a range of Newtonian and non-Newtonian fluids. Turbulent flow measurements (Re > 20,000) are made using Newtonian fluids. Data from both techniques are compared in terms of average flow field and, where appropriate, turbulent fluctuating velocity components. Particular emphasis is given on how comparisons can be made between the Eulerian PIV data and the Euler-Lagrangian PTV data. The overall results demonstrate the validity of the PTV technique in this application to acquire average flow fields which are in good agreement with PIV. Turbulent flow properties are less well resolved by PTV due in part to the large size of the tracer particle used. Other advantages and limitations of PTV versus PIV are also discussed.

1. Introduction

3-D Particle Tracking Velocimetry (PTV) is a flow measurement technique which is currently used in industrial environments due to its versatility compared to 2-D Particle Image Velocimetry (PIV) systems, though they are closely related (Adrian, 1991; Willert and Gharib, 1991). A key advantage is the use of visible light rather than laser-based illumination which substantially reduces both cost and health and safety requirements. The development of the PTV technique arises from advances in hardware and image processing algorithms in the last few decades particularly via activities led by the Institute of Geodesy and Photogrammetry at ETH Zurich. The development of 3-D PTV has been carried out in conjunction with photogrammetry (Willneff and Wenisch, 2011) which embraces a wide number of research areas including measurements from photographs (sonar, radar, lidar, etc.).

The camera records the 2-D position of light scattered from seeding particles which appear as point sources on a single image (Gao et al., 2012). The sizes and locations of the particles in the image can thus be related directly to the 2-D positions of the individual particles in the imaged plane, via an appropriate calibration. Using sequential images, particles may be tracked in space and time, yielding whole-field velocity information (Maas et al. 1993). As for the PIV technique, a critical requirement is the minimisation of optical distortions between the image plane and the camera lens, for example by matching of the refractive index

* Corresponding author.
E-mail address: f.alberini@bham.ac.uk (F. Alberini).

http://dx.doi.org/10.1016/j.ces.2017.05.034
0009-2509/

between the external wall (glass or Perspex) and the fluid, and elimination of curvature.

The camera calibration is critical for accurate 3-D PTV measurements (Willneff and Wenisch, 2011). This process determines the parameters which map 3-D points within a certain scene or object onto their corresponding 2-D projections in the camera image. Many methodologies have been developed for camera calibration with linear, nonlinear and two-step optimization schemes to model camera parameters which may include lens distortion effects (Hall et al. (1982), Luong and Faugeras (1997), Tsai (1987), Jin et al. (2006)).

The calibration is divided into three steps. The first step, called camera modelling, involves the mathematical approximation of the physical and optical behaviour of the camera sensor by using a set of parameters. The second step deals with the use of direct or iterative methods to estimate the values of these parameters. A limitation is the available camera memory which limits the capture time. Stuer et al. (1998) considered how image compression could reduce this issue. The third and final step for the correct acquisition of data is image processing which is used to determine the 3-D particle position. Kieft et al. (2002) demonstrates the efficiency of the 3-D localisation algorithm to track the particle in a 3-D space which is based on the work of Bastiaans et al. (2002). Firstly, the captured images are dynamically thresholded, then, within each image, the 2-D representation of a particle is detected. Finally, from the particles located in the different planes, a 3-D position can be deduced by a mapping process driven by the 3-D localisation algorithm. As soon as the 3-D position of the particles is known in each set of images, the procedures for obtaining their velocity are equivalent to those used in 2-D PIV.

The 3-D particle-tracking velocimetry (PTV) algorithm has been tested to prove its accuracy and performance by Willneff and Wenisch (2011). They found that the algorithm can determine particle position with an accuracy of less than half of the particle diameter. The performance tests show that for particles located in a 2-D plane, the algorithm can track particles with a vector yield reaching 100%, which means that a velocity vector can be determined for almost all particles detected.

In the open literature, 3-D-PTV has been carried out using several different equipment configurations. For example, Hwang et al. (2007) used six cameras for the analysis of fluid interactions in an impinging jet. Full 3-D Euler-Lagrangian velocity fields were obtained by Monica et al. (2009) in their investigation of flow and transport in porous media. Krug et al. (2014) applied combined scanning PTV/LIF technique to simultaneously measure the full velocity gradient tensor and the 3-D density field in a gravity current facility. In their work two cameras have been used; one equipped with a cut off filter for the LIF and the other was mounted in front of a combination of mirrors. A single volumetric laser has been utilised to illuminate both particles and dye (at a different wavelength to the emitted fluorescent light) to enable simultaneous detection of the dye for LIF and the particles for PTV measurements.

Even though multiple cameras systems are effective and yield high quality results, the cost implications are obvious and prohibitive. Thus introduction of a single camera and mirror systems, as well as cost effective LED lighting have driven further popularization of 3-D-PTV. Willert and Gharib (1992) introduced a system for 3-D PTV using a single camera in combination with 4 mirrors (Pereira et al., 2006; Kreizer et al., 2010). This setup up allows the focusing of two projections of the same space in a single frame. In recent years, this system has been applied to reconstruct highly resolved blood flow patterns (Gulan et al., 2012; Gallo et al., 2014).

There is a lack of information in the literature of how 3-D PTV can be applied to processing applications such as the mixing of fluids within a stirred vessel, particularly for fluids with complex rheology. Previous work has used Positron Emission Particle Tracking (PEPT) to obtain the Lagrangian flow field in a stirred vessel (Fangary et al., 1999; Guida et al., 2010; Liu and Barigou, 2015) or 2-D PIV for the Eulerian flow field (Aubin et al., 2004; Hall et al., 2005; Chung et al., 2009; Gabriele et al., 2011; Makowski and Baldyga, 2011; Fontaine et al., 2013; Montante et al., 2013).

Comparisons between 3-D PTV and techniques such as 3-D PIV (Atkinson et al., 2013) and Tomo-PIV (Kim et al., 2013), can be found in the literature. Atkinson et al. (2013) compared the two techniques in terms of hardware performance, observing no single method proves optimal in terms of all factors including formation, saving, loading, storage size and the extraction of intensity windows or individual particle information. The need to repeat PIV and PTV measurements places a significant importance on the time each method takes to extract a given intensity window or particle.

Kim et al. (2013) observed considerable differences between the two techniques when a measurement of the steady flow in a droplet was performed. The main differences were found to be that the 3-D particle distributions in the volume obtained by 3-D-PTV varied with the droplet height, while Tomo-PIV gives constant 3-D particle distributions over the depth. Other issues found were that for 3-D-PTV, the number of detected particles decreases with the distance to the wall, for both methods, but in different ways. For 3-D-PTV, the number of detected particles decreases, whereas in Tomo-PIV, the reconstructed particle intensity drops. The depth variation in the particle reconstructions of both methods is caused by the particles becoming increasingly out of focus with distance from the interface, which increases their size and decreases their peak intensity on the image. Other works investigate the measurement of turbulence using PTV focussing in jets (Fu et al., 2016; Kim et al., 2016).

The above literature review has outlined the challenges inherent in the application of 3-D PTV, nevertheless it remains an attractive option in terms of cost and potential for industrial applications. This paper is concerned with the application of 3-D PTV to obtain the flow of fluids within agitated stirred vessels, an application which is ubiquitous within the chemicals and manufacturing industries. The experimental investigation is made over low transitional, transitional and turbulent flow regimes using a range on Newtonian and non-Newtonian fluids. A direct comparison is made between 2-D PIV and 3-D PTV to demonstrate the consistency and accuracy of the Euler-Lagrangian velocity field obtained for the mixing of complex fluids. This work aims to identify the capabilities and benchmark the use of single camera 3-D PTV to assess the mixing performance in a batch stirred vessel.

2. Materials and methods

2.1. Stirred vessel

Fig. 1 shows the schematic of the stirred vessel used in both 2-D PIV and 3-D PTV experiments. The borosilicate glass vessel has a diameter $T = 190$ mm, and is filled with fluid to a height $H = 190$ mm (H/T = 1). The vessel was equipped with 4 vertical rectangular baffles located at 90° from each other around the vessel circumference with a width (B) of 0.02 m (B/T = 0.11). A down pumping 6-blade pitched blade turbine impeller (PBT6-60-DP) of diameter D = 105 mm (D/T = 0.55), was located on the tank axis, and the clearance (C) between the impeller and the bottom of the tank was 50 mm (C/T = 0.26; C/D = 0.48). The shaft was connected to an Heidolph overhead stirrer. The same geometry was used for all experiments.

2.2. Fluids and flow conditions

Five different fluids were used and their rheological properties are given in Table 1. Three Newtonian fluids were used comprised

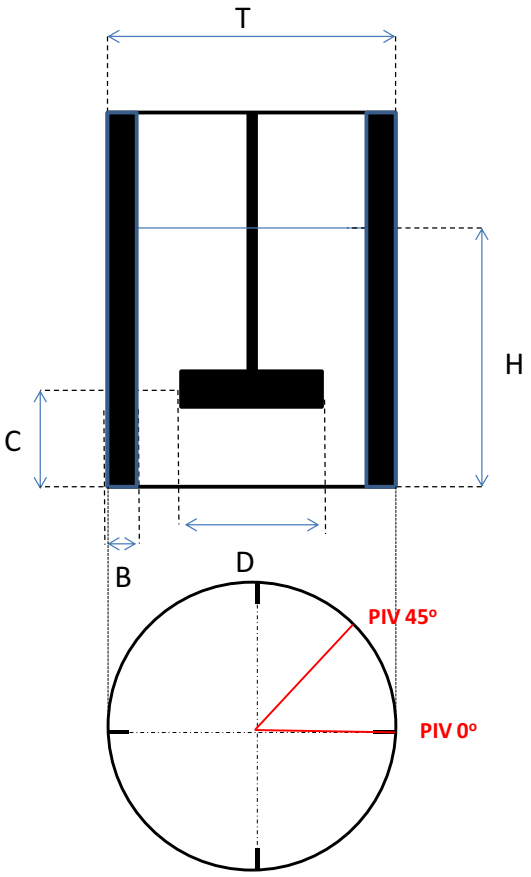

Fig. 1. Schematic of the stirred vessel.

of water and two water-glycerol mixtures at different glycerol concentrations (70%wt. and 98%wt). The two non-Newtonian fluids used were aqueous solutions of Carbopol 940 NF; 0.1%wt. at pH = 5 and 0.2%wt at pH = 4.5.

The rheological properties of the fluids were obtained at room temperature (20 °C) using a controlled stress rheometer (HR-2, TA instruments) equipped with a 60 mm diameter 2° cone and plate geometry. The rheology of the non-Newtonian fluids can be described using the Herschel-Bulkley constitutive law (Alberini et al., 2014)

$$\tau = \tau_o + K\dot{\gamma}^n, \tag{1}$$

where values of the yield stress, τ_0, consistency index, K, and power law exponent, n, are given in Table 1.

The flow conditions used for the experiments were determined based upon the Reynolds number. For the Newtonian cases Reynolds number was calculated using

$$\mathrm{Re} = \frac{\rho N D^2}{\mu}, \tag{2}$$

where μ is the viscosity at fixed temperature, ρ is the density and N is the impeller rotational speed.

For non-Newtonian fluids, an apparent average shear rate ($\bar{\dot{\gamma}}$) has been calculated based on the Metzner Otto relationship (Metzner and Otto, 1957),

$$\bar{\dot{\gamma}} = k_s N, \tag{3}$$

where the Metzner-Otto constant, k_s, for a down pumping PBT has a value of 13 (Paul et al., 2004). Using the Herschel-Bulkley model (1) the Reynolds number, Re, can thus be obtained using (Wassmer and Hungenberg, 2005):

$$\mathrm{Re} = \frac{\rho k_s N^2 D^2}{\tau_y + k(k_s N)^n} \tag{4}$$

The calculated Reynolds numbers and impeller rotational speeds for the flow condition/fluid combinations used in this work are given in Table 1. The impeller speeds for Newtonian fluids have been chosen to achieve a turbulent regime in water (Re = 33,000), high transitional regime in 70%wt. glycerol-water solution (Re = 1000) and low transitional regime (Re = 74) in 98%wt. glycerol-water solution. The impeller speeds for the non-Newtonian fluids have been set to match the values of Reynolds numbers in the low and high transitional regimes obtained with the Newtonian fluids, thus the 0.1%wt. Carbopol solution is used in the high transitional regime and the 2%wt. Carbopol solution is used in the low transitional regime.

2.3. Particle Image Velocimetry (PIV)

The 2-D PIV measurements were performed using a TSI PIV system (TSI Inc, USA). The system comprises a 532 nm (green) Nd-Yag laser (Litron Nano PIV) pulsing at 7 Hz, synchronized to a single TSI Power view 4MP (2048 × 2048 pixels^2) 12 bit CCD camera using a synchronizer (TSI 610035) attached to a personal computer. The PIV system was controlled using TSI Insight 4G software. For the angle-resolved measurements, an external optical trigger was used. A metal indicator rod was attached to the shaft which was aligned with the appropriate position of the impeller blade. An optical detector was mounted close to the shaft; when the indicator rod passed the detector with each rotation an electrical impulse passed into the synchroniser which triggered the PIV measurement. Thus, measurements were made at the same blade angular (azimuthal) position.

The spatial resolution of the measurements was 100 μm pixel^{-1}. Insight 4G software was used to process the data and generate the spatial velocity fields. For each experiment, 500 images were captured and combined to determine the average flow field. The velocity fields were obtained using the Nyquist PIV algorithm developed by TSI. The interrogation area was set at 64 × 64 pixels and to identify the single particles in the image the Gaussian peak method was applied (Westerweel, 1997). The magnitude of the velocity vectors in Cartesian co-ordinates are defined as u_r and u_z respectively. Since the vertical plane of interest is along the vessel

Table 1
Rheological properties of non-Newtonian solutions and flow conditions.

Solution	Yield stress, τ_0 (Pa)	Consistency index, K (Pa s)	Power law exp., n (–)	Rotational speed, N (rpm)	Reynolds number, Re (–)	Flow regime
0.1%wt Carbopol 940 NF	1.47	1.03	0.40	450	1000	*High transitional*
0.2%wt Carbopol 940 NF	13.11	5.41	0.43	300	74	*Low transitional*
	Viscosity (μ) at 20 °C [Pa s]					
Glycerine 70%wt	0.02			110	1000	*High transitional*
Glycerine 98%wt	0.95			300	74	*Low transitional*
Water	0.001			180	33,000	*Turbulent*

axis, the *x* direction and *y* direction map onto the radial and axial directions within the vessel respectively.

Two specific planes of the vessel were investigated as shown in Fig. 1. An angle of 0° refers to when the baffle is just behind the image plane (by ca. 1 mm) allowing the laser sheet to travel undisturbed avoiding reflections; these measurements enable the local influence of the baffle to be elucidated. An angle of 45° between the baffles is also chosen. These are denoted PIV 0 and PIV 45 in the figure.

2.3.1. 3-D Particle Tracking Velocimetry (PTV)

For the PTV set-up, four LED lights (Marathon multiLED LT) were used, two on either side of the stirred tank on top of each other to illuminate the whole height of the vessel. Four mirrors are mounted between the stirred tank and a high speed camera (Photron SA4) so that the high speed camera is able to capture raw images simultaneously from both sides of the tank covering a 140° field of view, as shown in Fig. 2a. An example of a raw image from PTV measurement is shown in Fig. 2b.

Fluorescent green polyethylene microspheres with a size range of 180 – 212 μm were used as tracer particles. For the entire set of experiments, it was assumed that the flow was Stokesian $\tau_p/\tau_f < 1$ where τ_p and τ_f are the relaxation times of the particle and fluid respectively. τ_p is defined as $\rho_p d_p^2/18\mu_f$ which is approximately 2.2×10^{-2} s for the low Newtonian viscous fluid down to 2.7×10^{-6} s for the high Newtonian viscous fluid. τ_f is calculated as the ratio between impeller diameter and velocity of the impeller tip which ranges from 0.10 s to 0.04 s from the less viscous to the more viscous fluid used. Those numbers give Stokes numbers in the range between of 0.02 to 6×10^{-5}; which are conservative given that the actual fluid velocities are less than the impeller tip speed. These values of the Stokes number will occur at the tip of the impeller where velocities are highest and τ_f is at its lowest. However, this definition of τ_f is valid only for large scale turbulence which corresponds to the mean average flow. If the small scale turbulence is considered, τ_f is defined as $(\nu/\varepsilon)^{1/2}$ which corresponds to the Kolmogorov time scale (Kolmogorov, 1941). The Stokes number is this case is 2.88. The consequence of this high value will be discussed in light of the results below.

In order to achieve 3-D flow field reconstruction, a calibration target, as shown in Fig. 2c, is used to provide the 3-D coordinates from the 2-D images obtained. This, and the reconstruction software below, were both obtained from Photrak AG, Zurich, CH (http://www.photrack.ch/). The acquisition rate of the images was set at 1000 frames s^{-1} with a resolution of 200 μm $pixel^{-1}$. Due to camera memory limitation, 5457 raw images were obtained for each experimental condition which corresponds to ~5.45 s of recording.

The 3-D PTV algorithm from Photrak AG (Hoyer et al., 2005), was employed for the reconstruction of the 3-D flow field. Particle positions in polar coordinates (r, ϑ, z) in the raw images were detected and determined, and particle trajectories were obtained by tracking the particles thereafter. Different criteria used by the particle tracking techniques to find the corresponding particle position in the sequential image space and object space are discussed by Willneff (2002). In the present work, a 3-D search volume whose size depends on the minimum and maximum velocity was used as the criterion (Willneff, 2002). Finally, in order to carry out Eulerian analysis so that velocities can be compared with those from PIV, the whole measured domain (~2/5 of tank volume 140° angle field of view shown in Fig. 3) was divided into 30×50 square cells, i.e. in the radial (r) and axial (z) directions, respectively to obtain the azimuthally averaged data. Time-averaged velocity in each cell was obtained by

$$u_{AVG_{cell}} = \frac{\sum_{i=1}^{n} u_i}{n} \tag{5}$$

and fixing an arbitrary point r = R and z = Z, the radial and axial components of the velocity were obtained by

$$u_r = \frac{\sum_{i=1}^{n}\sum_{\vartheta=0}^{140} u_r(R,Z,\vartheta)}{n} \tag{6}$$

$$u_z = \frac{\sum_{i=1}^{n}\sum_{\vartheta=0}^{140} u_z(R,Z,\vartheta)}{n} \tag{7}$$

where n is the number of particles passing the cell and u_i is the velocity of each particle in the cell. In Fig. 3 an example of the top view of the vessel is shown. Each dot corresponds to a particle and the different colours indicate the different magnitude of the velocity. In some parts of the cross section shown in Fig. 3, the particles are not depicted due to the presence of shadows. The baffles used in this work are transparent but if they appear in the image their projection can create some shadow since the fluids and baffle material are not perfectly refractive index matched. Thus in these regions no particles are detected.

3. Results and discussion

3.1. Statistical validation of PTV versus PIV

Since PTV provides 3-D data in a fluid volume and 2-D PIV provides 2-D data within an imaging plane, some data treatment is necessary to enable comparison to be made. The first step is to reduce the PTV data into a single *r-z* plane by averaging the velocities obtained for each *r-z* coordinate in the azimuthal direction, i.e. the azimuthal co-ordinate values of velocity are collapsed into a single averaged value. The data could be treated by splitting into a series of vertical planes at fixed azimuthal angles however the sparsity of the data set, limited by the recording and processing time set in the hardware, prevent this being carried out. Thus the collapse of the azimuthal co-ordinate provides the best approach for comparison with the 2-D PIV data. However, there are some additional considerations to take into account, before the two are compared. For the azimuthally averaged PTV data, the mean flow field calculated in each cell (eq.3), is influenced by two factors with respect to the particle position; firstly the position of the baffles within the 140° field of view and secondly the position of the impeller blade, which is random since the PTV system does not resolve the flow fields with respect to blade angular position.

In the 2-D PIV measurements, the data have been obtained using time-averaged data over the 500 image pairs, obtained at either PIV 0 or PIV 45 positions with respect to the baffle, but not resolved by blade angular position (AVG), and data taken where the external trigger has been used to resolve the data by blade angular position, again at either PIV 0 or PIV 45 baffle positions (AR). The AR data are also time-averaged over the 500 image pairs.

One might expect that the best agreement between PTV and PIV would exist when comparing the AVG PIV data with the azimuthally averaged PTV data since the blade position in both data sets is random. However, the relative sparsity of the PTV data could in principle lead to discrepancies when compared to the 2-D PIV data, not in the least because data were not obtained for all 360° of the stirred vessel using PTV (see Fig. 3). In Fig. 4 all four options are explored in the turbulent regime by comparing the PIV data from the four cases outlined above, i.e.

- PIV 0 AVG: time averaged data obtained over 500 image pairs with random blade angular position, baffle angle of 0°.
- PIV 0 AR: time averaged data obtained over 500 image pairs with fixed blade angular position, baffle angle of 0°.

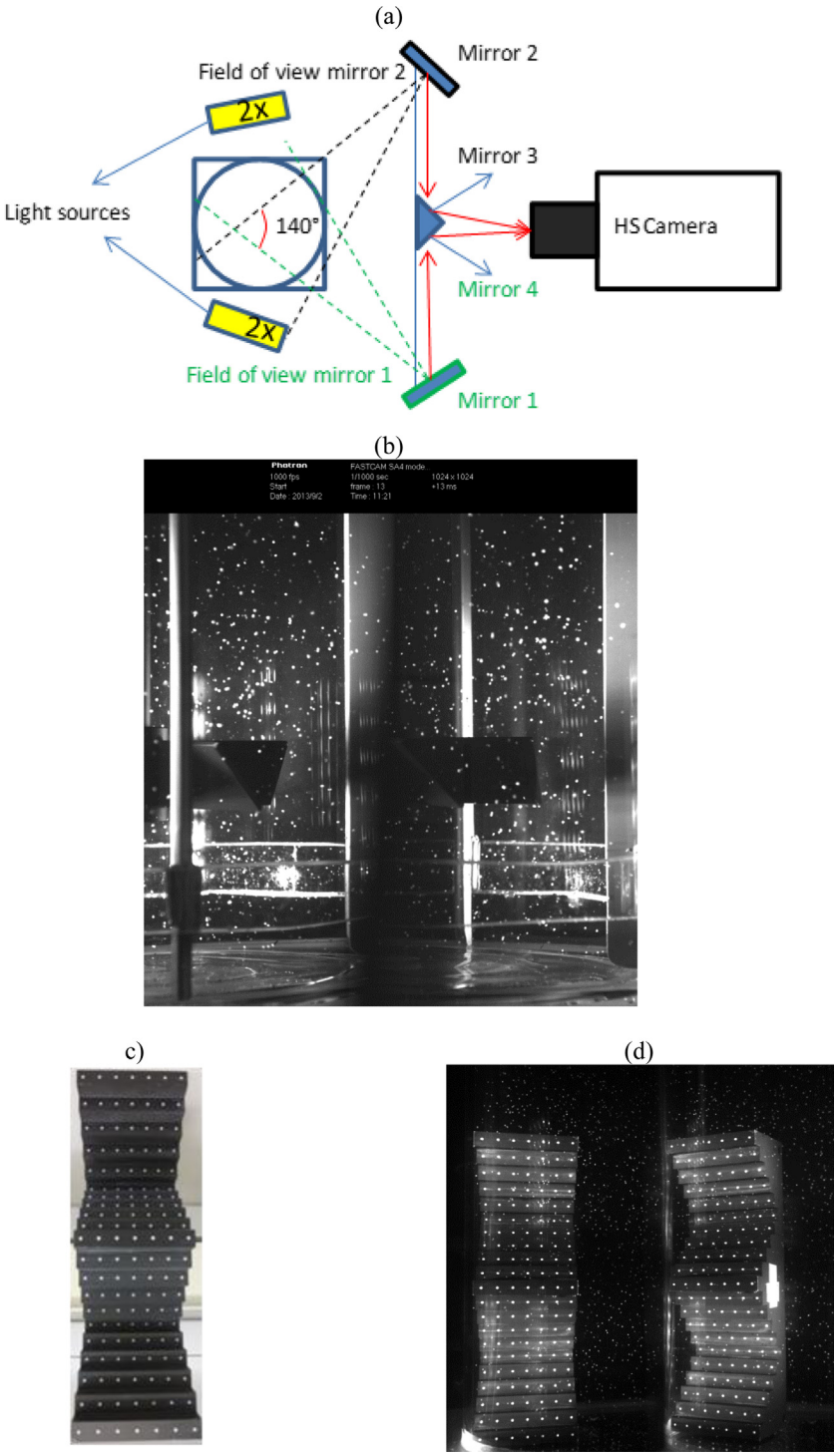

Fig. 2. PTV rig: (a) Schematic of PTV set up using mirrors and one camera, (b) example of raw PTV image acquired by HS camera and (c) calibration target and (d) calibration raw image.

- PIV 45 AVG: time averaged data obtained over 500 image pairs with random blade angular position, baffle angle of 45°.
- PIV 45 AR: time averaged data obtained over 500 image pairs with fixed blade angular position, baffle angle of 45°.

Comparing the two sets of AVG versus AR data in Fig. 4 it can be observed that the differences are limited. This is due to the impeller configuration used (6 blade PBT with 60° angled blades) which generates a flow field which is not much affected by the blade position (Gabriele et al., 2011). However, the effect of baffle position is very significant, with a small circular flow loop formed by the down-pumping impeller close to the discharge for a baffle position of 0°; this loop becomes elongated vertically to encompass the bottom half of the tank at a baffle position of 45°.

Given the above observations, the comparison against the PTV has been made using the angle resolved results at both baffle positions (PIV 0 AR and PIV 45 AR) by choosing the most extreme options available. This has been done since it allows the true turbu-

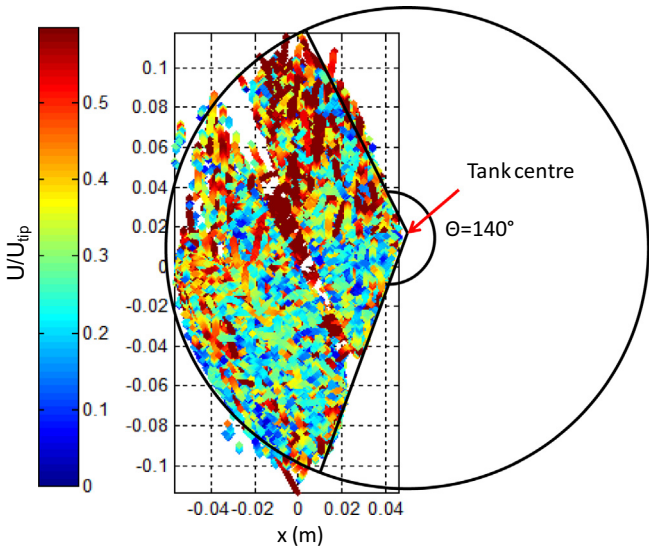

Fig. 3. Top view of the vessel showing the domain area measured in the radial direction.

lent fluctuations to be resolved from the PIV data since the periodic component of the fluctuating velocity due the passage of the blade has been removed (Gabriele et al., 2011).

Fig. 5a shows the flow pattern in the turbulent regime in detail for the PTV azimuthally averaged data (Re = 33,000 using water at an impeller speed N = 180 rpm). The velocity magnitude is normalized by the impeller tip speed of 0.98 m s^{-1}. The normalized axial position (axial coordinate divided by the fill height) is plotted versus the radial position (radial coordinate divided by the radius of the tank). The flow pattern is typical for a mixed flow down-pumping impeller, with a single downward flow loop emerging from the impeller discharge. The flow loop turns towards and flows upwards close to the vessel wall, before returning to the impeller region. A small circular secondary flow loop is observable in the bottom right of the image. This flow pattern is very similar to the one found in Guida et al. (2010) work for a similar PBT down pumping impeller. The corresponding particle density map is shown in Fig. 5b; this shows the number of separate particle velocity measurements taken at each *r-z* coordinate in the collapsed data. High densities correspond to high velocity regions; since the particle travels more quickly through these regions there is a higher probability of it returning within a fixed measurement time period. Thus the probability of a particle being seen in the same cell is proportional to the particle velocity.

To enable validation of the PTV data, the flow statistics are examined by choosing three points in the vessel shown in Fig. 5a which cover the extremes of the flow behaviour: sample point 1 is positioned in the impeller discharge, point 2 is close to the fluid free surface where the flow is relatively weak and point 3 is located next to the wall. It is well known that to achieve statistically consistent PIV results in the turbulent regime, a minimum number of image pairs is required to ensure a stable average velocity and also a root stable mean square (rms) velocity. A similar analysis has thus been performed on the PTV measurements for the three different sample points. Both average and turbulent (Fig. 5b) velocities have been calculated as a function of the number of particles passing through the measurement points. The data are then compared with PIV results and plotted as a function of the number of processed image pairs.

For each sample point, the average velocity magnitude ($\frac{\bar{u}}{u_{tip}}$) is plotted versus the number of particles (PTV) or image pairs (PIV) normalized by the total number in Fig. 5b; recall that the total number of image pairs was 500 for the PIV for all three sample points. However, for the PTV the total number of particles varies, with a value of ~1000 for sample points 1 and 3 and ~700 for sample point 2 where the velocities are lower. It can of course be argued that the turbulence is lower where velocities, and hence the number of particles, are lower which compensates the statistics. Another issue known in Lagrangian methods is associated with data capture rate for high velocities. High velocities (close to the impeller tip) can be underestimated due to the rapid changes in both magnitude and direction (Chiti et al., 2011).

The data in Fig. 5b show that a stable average velocity value is always reached within ~150 pairs of image for PIV and ~300 particles for PTV at each sample point domain and the absolute values agreed within an error <15% A similar analysis has been performed

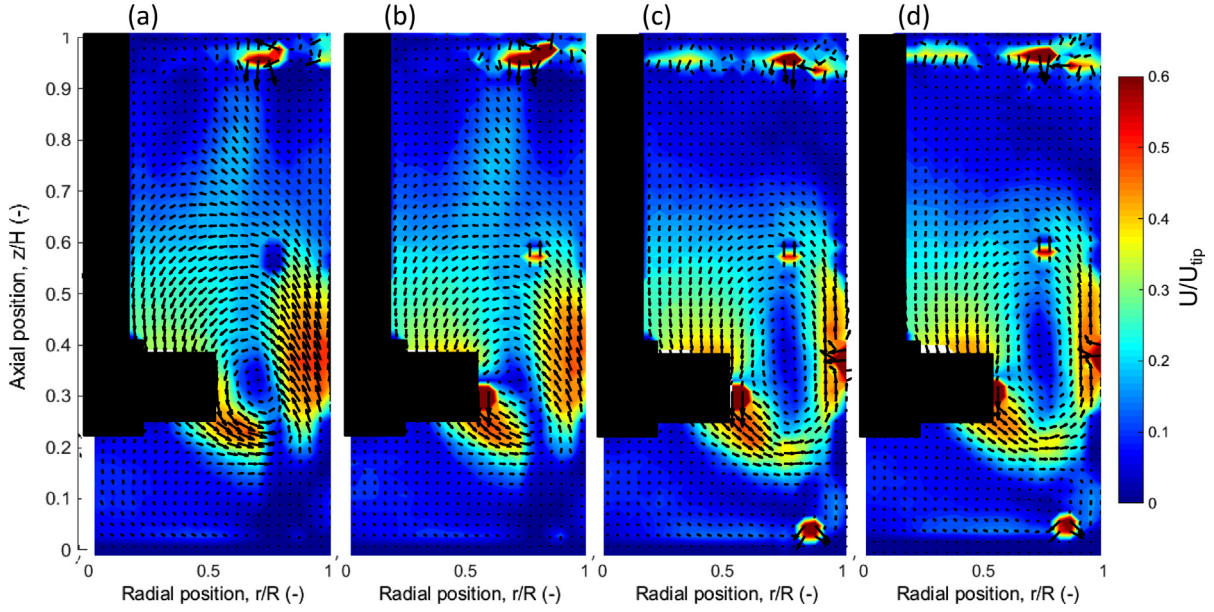

Fig. 4. PIV results in the turbulent regime for the four acquisition methods: for the plane at 0° to the baffle (a) ensemble average velocity field (PIV 0 AVG), (b) angle resolved velocity field (PIV 0 AR), for the plane at 45° to the baffle (c) ensemble average velocity field (PIV 45 AVG), (d) angle resolved velocity field (PIV 45 AR).

for the square of the rms velocities $u_r'^2$ (PIV) and $u_r'^2$ (PTV) shown in Fig. 5b.

PIV measurements show expected results which are plotted in Fig. 5b for each point. Again, the data show that stable square rms value within 95% confidence interval and it is always reached within ~500 particles for each sample point domain. The number of minimum pairs of images required varies as a function of the sample point position which is expected because close to the impeller the turbulence is higher (high fluctuation) than at the top of the vessel, thus the former takes longer to converge.

The PTV measurements show much lower values of the fluctuating velocity component and almost identical trends are observed for each of the three sample points. It should be noted that square of the rms values obtained from PTV are not representative of the true fluctuating velocity because they contain the periodic component due to the blade passage. Nevertheless, this does not explain the low obtained values which are most likely due to the large Stokes number for the PTV particles. Due to their relatively large size as described in §2.4, the particles are incapable of following the flow sufficiently well to resolve the turbulent scales which acts to smooth the velocity data obtained. However, PTV could potentially determine the turbulent velocity if smaller particles were used, but consequently a smaller volume of the vessel would have to be analysed to allow the camera to detect the smaller size particles.

3.2. Comparison of PTV and PIV velocity fields for Newtonian and non-Newtonian fluids

The average velocity fields for the turbulent flow case obtained by both PTV and PIV are compared in Fig. 6. Fig. 6a presents the flow maps obtained using PIV for PIV 0 AR, PIV 45 AR and using PTV (azimuthally averaged data). Similar results are observed between both techniques, with the best match between PIV 45 AR and PTV. This suggests that the flow loop structure away from the baffle persists through most of the vessel, with the changes in pattern observed at a baffle position of 0° being highly localised close to the baffle.

In Fig. 6b the normalized average velocities (u_z and u_r) obtained from PIV and PTV are plotted versus the radial position, r/R, where r is the radial position and R is the radius of the tank. Three different slices at constant z (z = 25 mm, ~H/8; z = 50 mm, ~H/4; z = 95 mm, ~H/2) have been chosen and the results show remarkable agreement, especially between PIV 45 AR and PTV. These results show that although the turbulent velocities cannot be captured satisfactorily by PTV, the average flow field is very well represented and the results from PTV can thus be used with confidence in this context.

The results presented in the following analysis describe the validation of PTV measurements for different flow regimes (low transient and high transient) and for Newtonian and non-Newtonian rheology fluids. A similar approach to the turbulent Newtonian case above is used. For each condition two flow maps (0° and 45°) of angle resolved PIV measurements and a single flow pattern contour plot of azimuthally averaged PTV measurements are presented as well as the trend of mean velocity for the three different horizontal slices taken at constant z coordinate.

Fig. 7a shows the low transient regime case (Re = 74), where a Newtonian fluid (Glycerol 98%wt) was stirred at 300 rpm. The maximum tip speed in this case is 1.65 m s^{-1}. Clearly, the results of the presented techniques show comparable outcomes. Again, the typical pattern of a down-pumping impeller can be observed from the vector field on the contour plots. The flow discharge starts close to the impeller and develops further next to the wall. As expected, the highest velocity magnitude values of U/U_{tip} are reached in the impeller discharge. Again, the PIV flow pattern at 45° baffle position matches closely the PTV results. The shape and magnitude of recirculation loops and stagnant areas are similar for all three measurements. Fig. 7b again shows good agreement for the three slices with the exception of z = 50 mm for the u_r where a more unstable behaviour is observed for the PTV data.

Fig. 8a shows the flow pattern in transient regime (Re = 1036), where a Newtonian fluid (Glycerol 70%wt) was stirred at 110 rpm. The maximum tip speed in this case is 0.39 m s^{-1}. The similarities between the different plots match the previous observations. As expected in transient conditions, the recirculation area increases compared to the low transitional case, due to the lower viscosity which enhances the momentum transfer in the system. Good agreement between the methods are shown in Fig. 8b for all slices and radial and axial velocities. These results show that

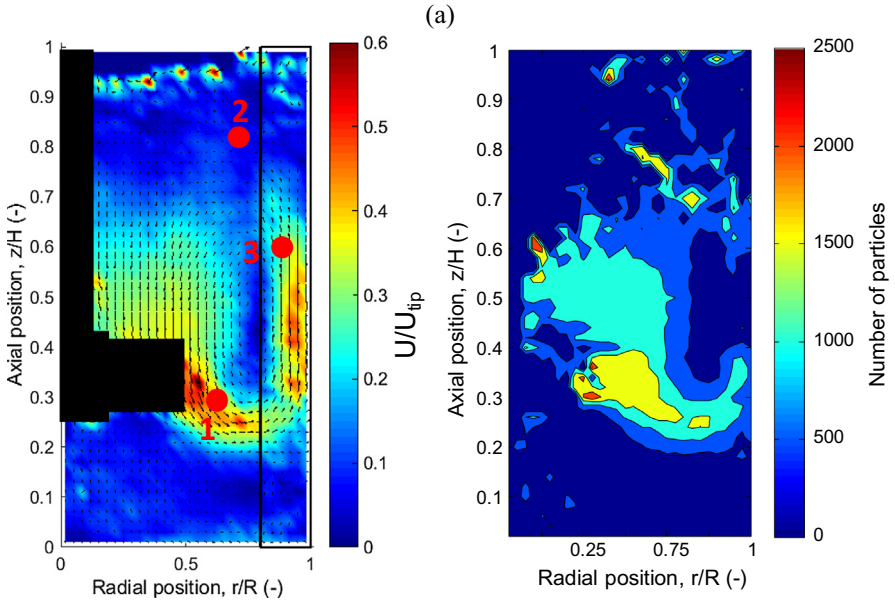

Fig. 5. Local comparison between PIV and PTV for turbulent regime: (a) Azimuthally PTV average velocity contour plot and locations of the three points used for the comparison. and density of particle for the turbulent PTV measurements. (b) Normalised Magnitude velocity and turbulent velocity plots at the three points for PIV and PTV measurements.

(b)

(1)

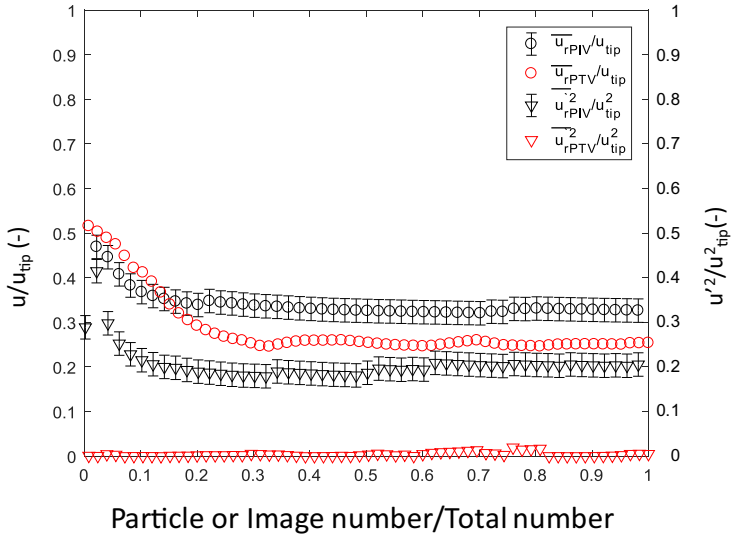

(2)

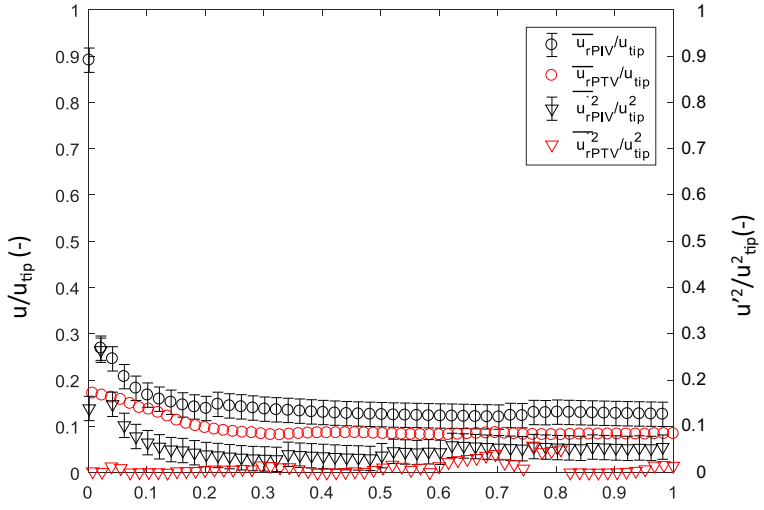

(3)

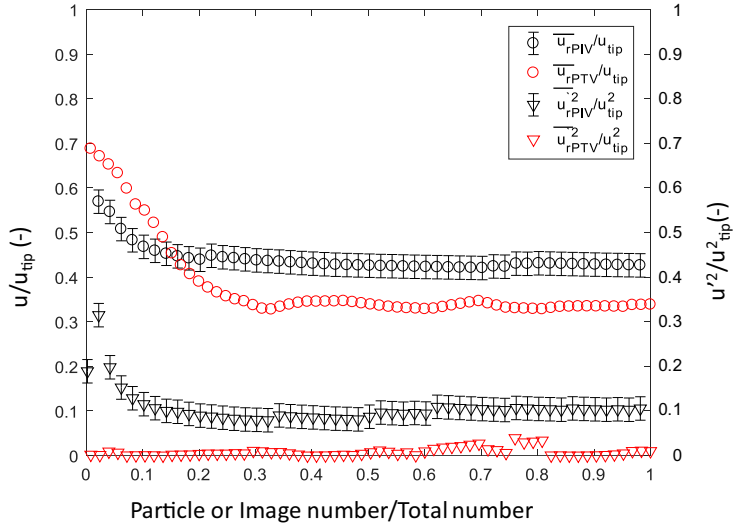

Fig. 5 (*continued*)

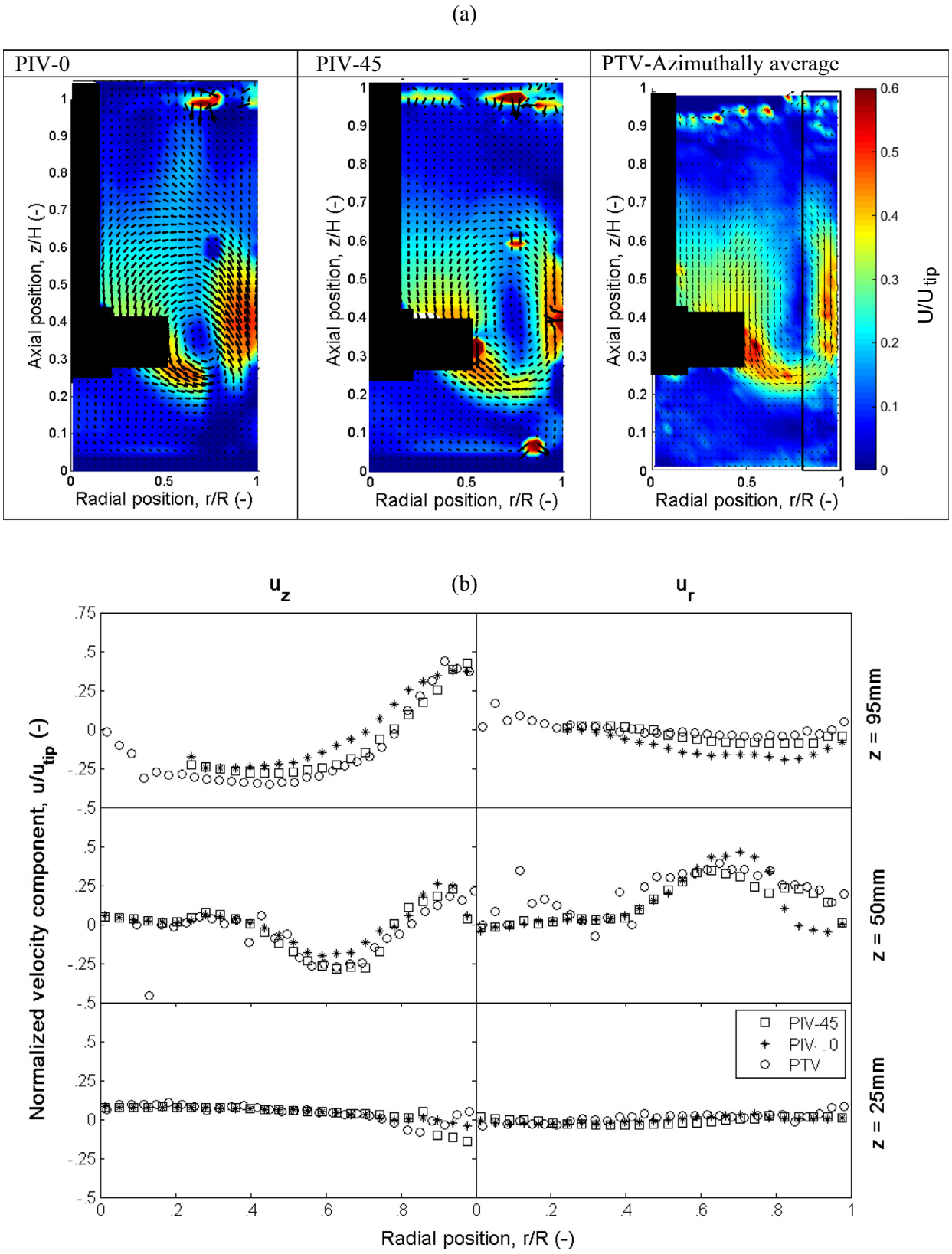

Fig. 6. (a) Flow pattern for Turbulent regime at Re = 33000 using water. Contour plot shows the no-dimensional U/U_{tip} and (b) Trend of normalized velocity in radial position for selected axial positions such as z = 95 mm (~H/2), z = 50 mm (~H/4) and z = 25 mm (~H/8).

PTV can be used reliably to obtain the average flow field in stirred vessels for Newtonian fluids in close to laminar (low transitional) and turbulent flow regimes.

Since the blending of non-Newtonian fluids attracts a lot of attention from industry, this study also explores the capabilities of PTV to perform fluid measurements in such systems. Non-

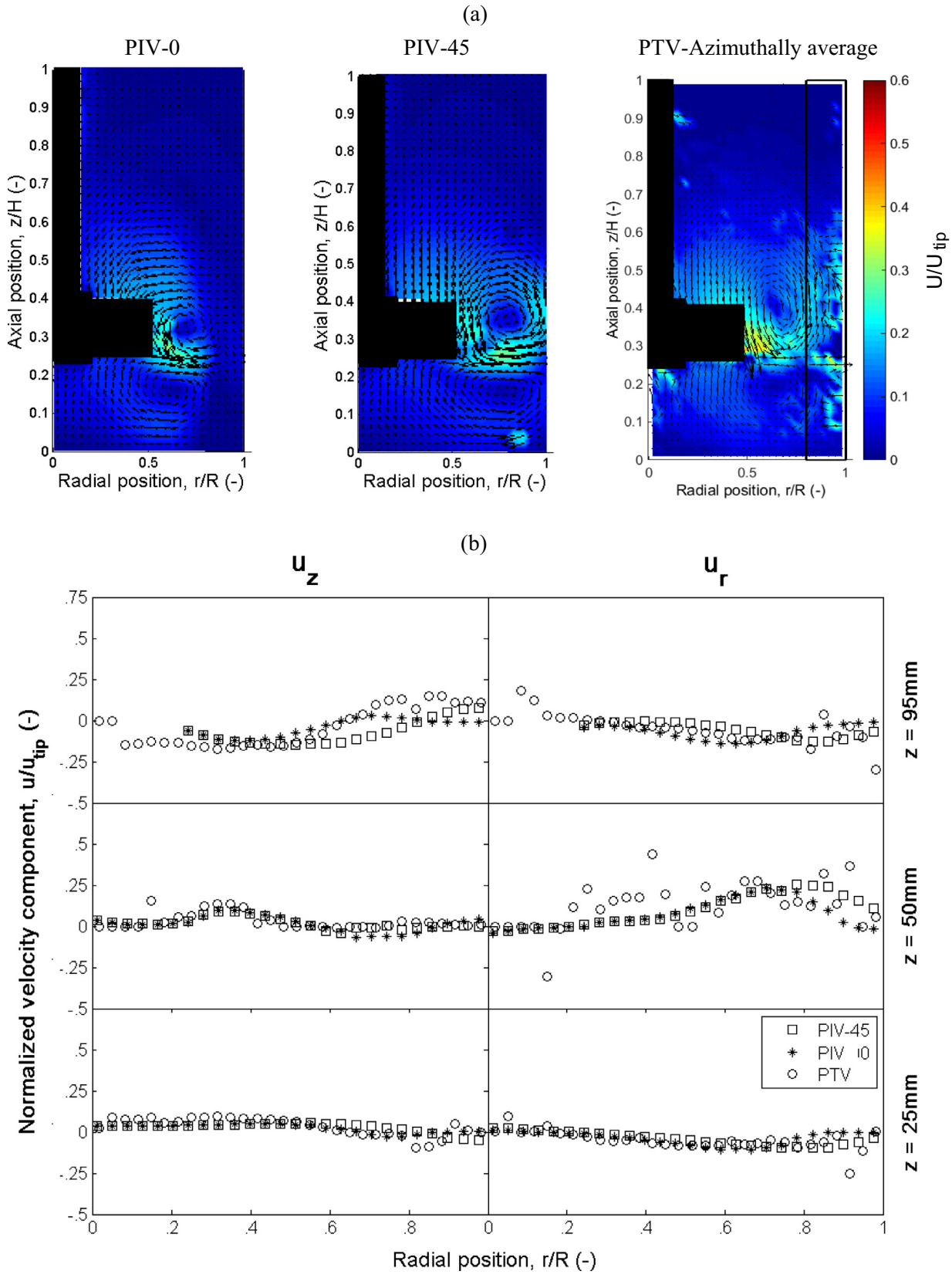

Fig. 7. (a) Flow pattern for Low Transitional regime at Re = 74 using Glycerine 98%wt. Contour plot shows the no-dimensional U/U_{tip} and b) Trend of normalized velocity in radial position for selected axial positions such as z = 95 mm (~H/2), z = 50 mm (~H/4) and z = 25 mm (~H/8).

Newtonian rheology can cause additional flow phenomena such as caverns (yield stress fluids) or pseudo-caverns (shear-thinning fluids) as well as phenomena induced by fluid normal stresses in viscoelastic fluids. In this work, the blending of a Herschel-Bulkley fluid (aqueous solutions of Carbopol 940 NF) has been carried out at values of Reynolds numbers equal to the low and high tran-

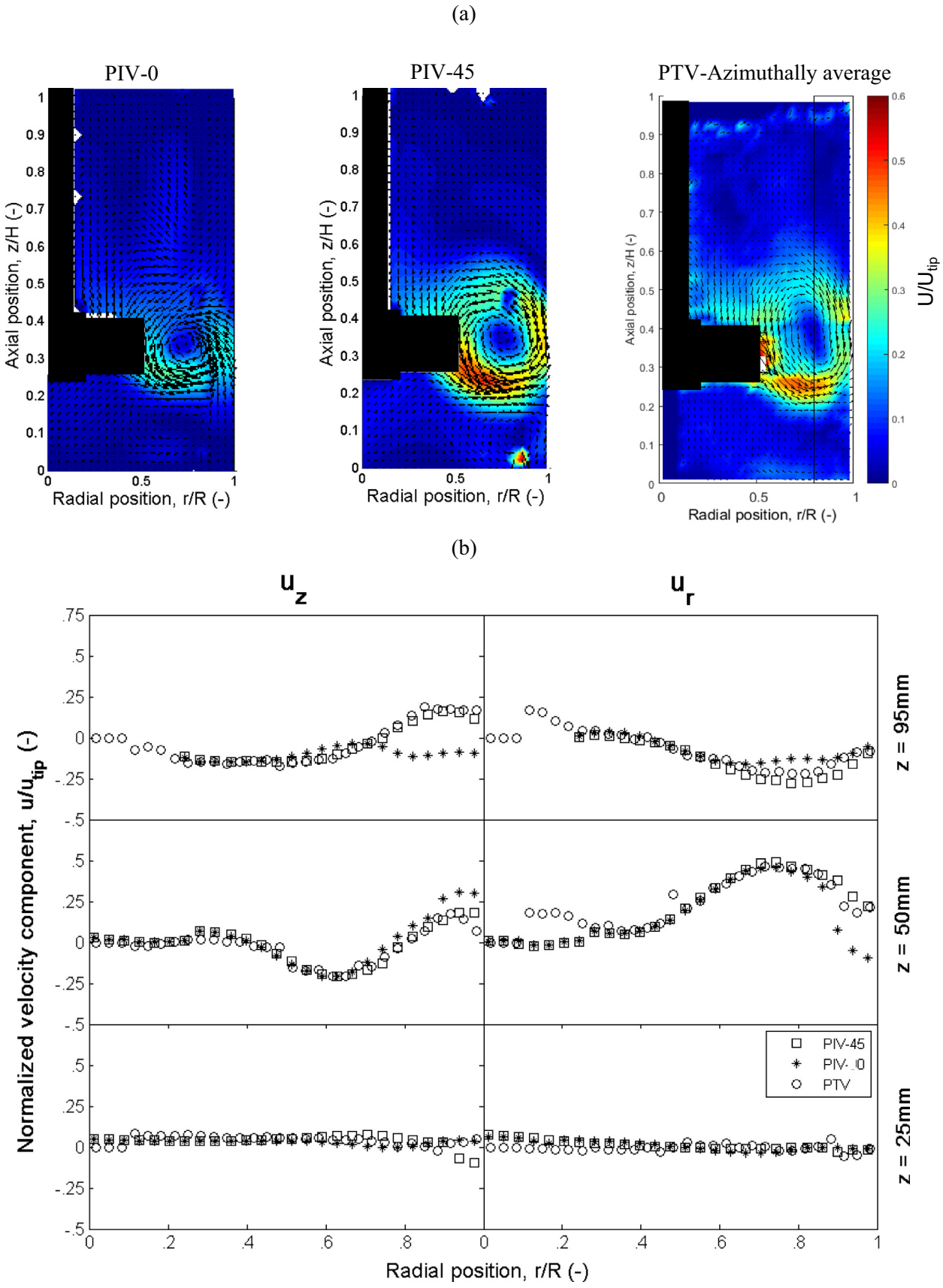

Fig. 8. (a) Flow pattern for High Transitional regime at Re = 1000 using Glycerine 70%wt. Contour plot shows the no-dimensional U/U_{tip} and (b) Trend of normalized velocity in radial position for selected axial positions such as z = 95 mm (∼H/2), z = 50 mm (∼H/4) and z = 25 mm (∼H/8).

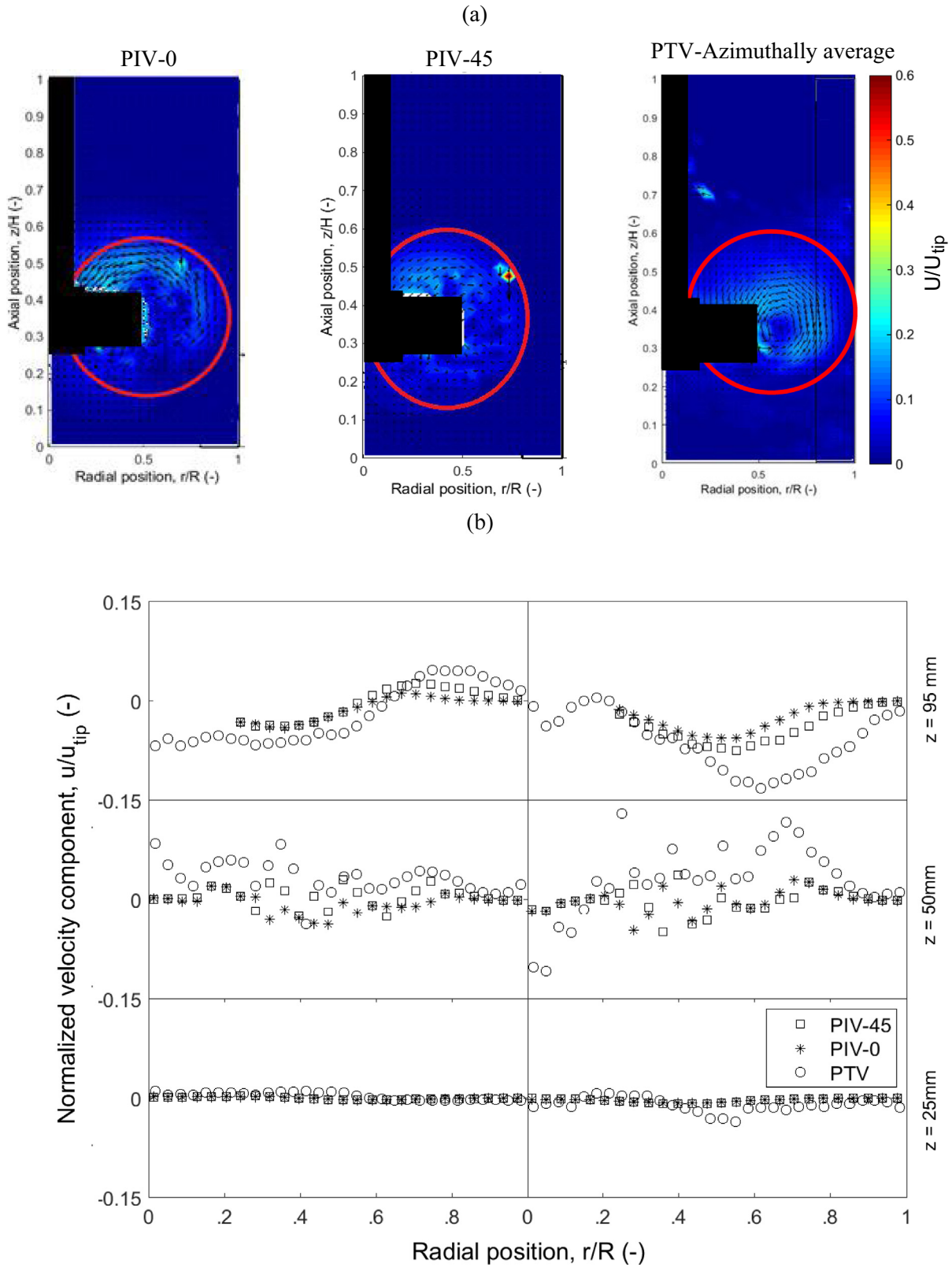

Fig. 9. (a) Flow pattern for Low Transitional regime at Re = 74 using 0.2%wt Carbopol 940NF solution. Contour plot shows the no-dimensional U/U_{tip} and (b) Trend of normalized velocity in radial position for selected axial positions such as z = 95 mm (~H/2), z = 50 mm (~H/4) and z = 25 mm (~H/8).

sitional regime cases chosen for the Newtonian fluids. It was not possible to investigate turbulent flow due to overload of the motor at the high rotational speeds required.

Fig. 9a shows the flow pattern in low transitional regime (Re = 74) using a solution of 0.2%wt. Carbopol 940NF. The tip speed is 1.65 m s^{-1}. As expected, the flow pattern is characterised

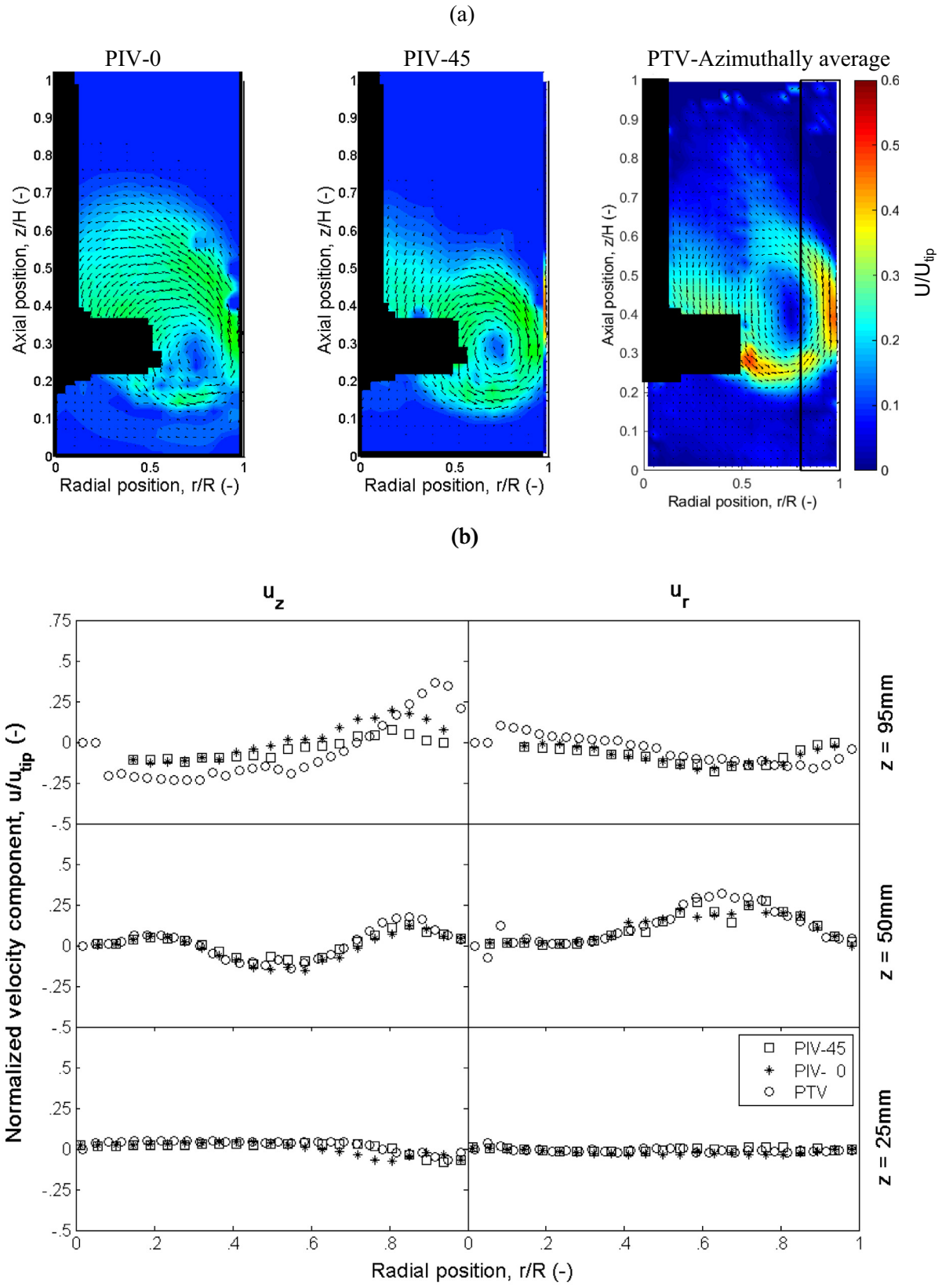

Fig. 10. (a) Flow pattern for High Transitional regime at Re = 1000 using 0.1%wt Carbopol 940NF solution. Contour plot shows the no-dimensional U/U_{tip} and (b) Trend of normalized velocity in radial position for selected axial positions such as z = 95 mm (~H/2), z = 50 mm (~H/4) and z = 25 mm (~H/8).

by the presence of a cavern which is due to the yield stress of the fluid (red line on Fig. 9a). Adams and Barigou (2007) in their work showed the presence of this cavern using a PBT down pumping impeller. The cavern increases in size with Re number and decrease in size at fixed tip speed with the increase of yield stress.

As for the Newtonian cases the flow pattern described by the 45° plane is closer to the PTV results. The main difference between the 0° and 45° plane is the size of the cavern because the presence of the baffle increases the size of the stagnant zone. The velocity magnitude is similar for all three plots and clearly the recirculation loop is confined between the discharge of the impeller and the zone above the blade, not below as for the Newtonian cases. The comparison of the trend of normalized velocity in radial position for selected axial positions is presented in Fig. 9b which shows consistent results between the two techniques.

The last case, shown in Fig. 10a, represents the high transitional flow regime (Re ∼ 1000) for non-Newtonian fluids where a solution of 0.1%wt. Carbopol 940NF is used. The tip speed is 2.47 m s^{-1}. As the previous non-Newtonian case, it can be seen clearer the formation of the cavern which is expected to be larger than before due to lower value of yield stress and higher tip speed (Adams and Barigou, 2007). Compared to the previous runs, the flow patterns between PIV and PTV are different in the absolute values of the velocity magnitude and it seems the PTV over estimates slightly the velocity in the cavern. However, the flow pattern of PTV is a combination between the PIV results for 0° and 45° baffle positions where the discharge zone is slightly higher than for the PIV results. Similar behaviour can also be seen for the Newtonian transient flow case (See Fig. 8a). Finally, similar trends can be seen for the normalized velocity as a function of radial position with some absolute values of velocity which are slightly overestimated by the PTV compared to PIV, in particular at the edge of the cavern. This is maybe due to not exactly the same position of the slice between the two set of data (PIV and PTV).

4. Conclusions

PIV and PTV measurements have been performed to determine the flow patterns generated by PBT down pumping impeller in a baffled stirred tank. Different flow regimes have been investigated using Newtonian and non-Newtonian fluids in particular focussing on low transitional and high transitional regimes. In addition, the turbulent regime is investigated for the Newtonian case. Typical flow patterns for Newtonian and non-Newtonian fluids have been shown using angle resolved data of PIV (0° and 45° angle) and azimuthally averaged data for the PTV.

The overall results show that the PTV is a valid technique to acquire flow field in a stirred tank and give results comparable with PIV in the r-z plane. Although the two techniques have comparable outputs, they have different and unique features such as 3-D information for PTV or angle resolved data for PIV. Flow in the tangential plane is not captured by the PIV and might be a useful future study. Generally, the comparison between PIV 45 AR and PTV agrees within a divergence less than 5%. An exception is the high transitional flow for non-Newtonian case where for z = H/2 the PTV data are slightly different compared to the other cases. However, all data points do not diverge more than 15% and are concentrated only in the discharge zone where the flow is more unstable in transient regime. Comparison between the PIV and PTV data for z = H/4 and z = H/8 is in strong agreement.

The difference in tracer particle size, ∼10 μm for PIV and ∼200 μm for PTV, affects the overall resolution of the measurements. For PTV, the scale of measurement is directly connected to the size of particles and calibration target which limits the capability of PTV to determine smaller turbulent scales. This is offset by the much lower cost of the PTV equipment if that capability is not required. In general, PTV seems appropriate for resolving the azimuthally-averaged mean velocity field but not turbulence quantities without further modification of the tracer particles used.

Acknowledgments

This research was supported by EMFormR project funded by InnovateUK and the Engineering and Physical Sciences Research Council (EP/L505766/1).

References

Adams, L.W., Barigou, M., 2007. CFD analysis of caverns and pseudo-caverns developed during mixing of non-newtonian fluids. Chem. Eng. Res. Des. 85, 598–604.
Adrian, R.J., 1991. Particle-imaging techniques for experimental fluid-mechanics. Annu. Rev. Fluid Mech. 23, 261–304.
Alberini, F., Simmons, M.J.H., Ingram, A., Stitt, E.H., 2014. Use of an areal distribution of mixing intensity to describe blending of non-newtonian fluids in a kenics KM static mixer using PLIF. AIChE J. 60, 332–342.
Atkinson, C., Buchmann, N.A., Soria, J., 2013. Computationally efficient storage of 3-D particle intensity and position data for use in 3-D PIV and 3-D PTV. Meas. Sci. Technol., 24.
Aubin, J., le Sauze, N., Bertrand, J., Fletcher, D.F., Xuereb, C., 2004. PIV measurements of flow in an aerated tank stirred by a down- and an up-pumping axial flow impeller. Exp. Thermal Fluid Sci. 28, 447–456.
Bastiaans, R.J.M., Van der Plas, G.A.J., Kieft, R.N., 2002. The performance of a new PTV algorithm applied in super-resolution PIV. Exp. Fluids 32, 346–356.
Chiti, F., Bakalis, S., Bujalski, W., Barigou, M., Eaglesham, A., Nienow, A.W., 2011. Using positron emission particle tracking (PEPT) to study the turbulent flow in a baffled vessel agitated by a Rushton turbine: improving data treatment and validation. Chem. Eng. Res. Des. 89 (10), 1947–1960.
Chung, K.H.K., Simmons, M.J.H., Barigou, M., 2009. Local gas and liquid phase velocity measurement in a miniature stirred vessel using PIV combined with a new image processing algorithm. Exp. Thermal Fluid Sci. 33, 743–753.
Fangary, Y.S., Seville, J.P.K., Barigou, M. 1999. Flow studies in stirred tanks by positron emission particle tracking (PEPT), Rugby, Inst Chemical Engineers.
Fontaine, A., Guntzburger, Y., Bertrand, F., Fradette, L., Heuzey, M.C., 2013. Experimental investigation of the flow dynamics of rheologically complex fluids in a Maxblend impeller system using PIV. Chem. Eng. Res. Des. 91, 7–17.
Fu, S., Biwole, P.H., Mathis, C., 2016. Numerical and experimental comparison of 3-D Particle Tracking Velocimetry (PTV) and Particle Image Velocimetry (PIV) accuracy for indoor airflow study. Build. Environ. 100, 40–49.
Gabriele, A., Tsoligkas, A.N., Kings, I.N., Simmons, M.J.H., 2011. Use of PIV to measure turbulence modulation in a high throughput stirred vessel with the addition of high Stokes number particles for both up- and down-pumping configurations. Chem. Eng. Sci. 66, 5862–5874.
Gallo, D., Gulan, U., di Stefano, A., Ponzini, R., Luthi, B., Holzner, M., Morbiducci, U., 2014. Analysis of thoracic aorta hemodynamics using 3-D particle tracking velocimetry and computational fluid dynamics. J. Biomech. 47, 3149–3155.
Gao, Q., Wang, H.P., Wang, J.J., 2012. A single camera volumetric particle image velocimetry and its application. Sci. China-Technol. Sci. 55, 2501–2510.
Guida, A., Nienow, A.W., Barigou, M., 2010. PEPT measurements of solid-liquid flow field and spatial phase distribution in concentrated monodisperse stirred suspensions. Chem. Eng. Sci. 65, 1905–1914.
Gulan, U., Luthi, B., Holzner, M., Liberzon, A., Tsinober, A., Kinzelbach, W., 2012. Experimental study of aortic flow in the ascending aorta via particle tracking velocimetry. Exp. Fluids 53, 1469–1485.
Hall, E.L., Tio, J.B.K., McPherson, C.A., Sadjadi, F.A., 1982. Measuring curved surfaces for robot vision. Computer 15, 42–54.
Hall, J.R., Barigou, M., Simmons, M.J.H., Stitt, E.H., 2005. A PIV study of hydrodynamics in gas-liquid high throughput experimentation (HTE) reactors with eccentric impeller configurations. Chem. Eng. Sci. 60, 6403–6413.
Hoyer, K., Holzner, M., Lüthi, B., Guala, M., Liberzon, A., Kinzelbach, W., 2005. 3-D scanning particle tracking velocimetry. Exp. Fluids 39, 923–934.
Hwang, T.G., Doh, D.H., Jo, H.J., Tsubokura, M., Piao, B., Kuroda, S., Kobayashi, T., Tanaka, K., Takei, M., 2007. Analysis of fluid-elastic-structure interactions in an impinging jet with a dynamic 3-D-PTV and non-contact 6D-motion tracking system. Chem. Eng. J. 130, 153–164.
Jin, S.Q., Fan, L.Q., Liu, Q.Y., Lu, R.S., 2006. Novel Calibration and Lens Distortion Correction of 3-D Reconstruction Systems. J. Phys: Conf. Ser. 48, 359.
Kieft, R., Schreel, K., van der Plas, G., Rindt, C., 2002. The application of a 3-D PTV algorithm to a mixed convection flow. Exp. Fluids 33, 603–611.
Kim, H., Westerweel, J., Elsinga, G.E. 2013. Comparison of Tomo-PIV and 3-D-PTV for microfluidic flows. Measurement Science & Technology, 24.
Kim, J.T., Zhang, Z., Liberzon, A., Zhang, Y., Chamorro, L.P., 2016. On the Lagrangian features of circular and semicircular jets via 3-D Particle Tracking Velocimetry. Exp. Thermal Fluid Sci. 77, 306–316.
Kolmogorov, A.N., 1941. Dissipation of energy in isotropic turbulence. Dokl. Akad. Nauk. SSSR 32, 19–21.
Kreizer, M., Ratner, D., Liberzon, A., 2010. Real-time image processing for particle tracking velocimetry. Exp. Fluids 48, 105–110.
Krug, D., Holzner, M., Luthi, B., Wolf, M., Tsinober, A., Kinzelbach, W., 2014. A combined scanning PTV/LIF technique to simultaneously measure the full velocity gradient tensor and the 3-D density field. Meas. Sci. Technol., 25.

Liu, L., Barigou, M., 2015. Lagrangian particle tracking in mechanically agitated polydisperse suspensions: multi-component hydrodynamics and spatial distribution. Int. J. Multiph. Flow 73, 80–89.
Luong, Q.T., Faugeras, O.D., 1997. Self-calibration of a moving camera from point correspondences and fundamental matrices. Int. J. Comput. Vision 22, 261–289.
Maas, H.G., Gruen, A., Papantoniou, D., 1993. Particle tracking velocimetry in three-dimensional flows. Exp. Fluids 15, 133–146.
Makowski, L., Baldyga, J., 2011. Large Eddy simulation of mixing effects on the course of parallel chemical reactions and comparison with k-epsilon modeling. Chem. Eng. Process. 50, 1035–1040.
Metzner, A.B., Otto, R.E., 1957. Agitation of non-Newtonian fluids. AIChE J. 3 (1), 3–10.
Monica, M., Cushman, J.H., Cenedese, A., 2009. Application of Photogrammetric 3-D-PTV technique to track particles in porous media. Transp. Porous Media 79, 43–65.
Montante, G., Magelli, F., Paglianti, A., 2013. Fluid-dynamics characteristics of a vortex-ingesting stirred tank for biohydrogen production. Chem. Eng. Res. Des. 91, 2198–2208.
Paul, E.L., Atiemo-Obeng, V.A., Kresta, S.M., 2004. Handbook of Industrial Mixing – Science and Practice. John Wiley & Sons, Chapter 6 page 370.
Pereira, F., Stuer, H., Graff, E.C., Gharib, M., 2006. Two-frame 3-D particle tracking. Meas. Sci. Technol. 17, 1680–1692.
Stuer, H., Willneff, J., Maas, H.G., 1998. Evaluation of image compression in 3-D PTV. In: Elhakim, S.F. Gruen, A. (Eds.) Videometrics Vi.
Tsai, R.Y., 1987. A versatile camera calibration technique for high-accuracy 3-D machine vision metrology using off-the shelf TV cameras and lenses, IEEE Int. J. Robot. Automat., RA-3, pp. 323–344.
Wassmer, K.H., Hungenberg, K.D., 2005. A unified model for the mixing of non-Newtonian fluids in the laminar, transition, and turbulent region. Macromol. Mater. Eng. 290, 294–301.
Westerweel, J., 1997. Fundamentals of digital particle image velocimetry. Meas. Sci. Technol. 8, 1379–1392.
Willert, C.E., Gharib, M., 1991. Digital particle image velocimetry. Exp. Fluids 10, 181–193.
Willert, C.E., Gharib, M., 1992. Three-dimensional particle imaging with a single camera. Exp. Fluids 12, 353–358.
Willneff, J., 2002. 3-D Particle Tracking Velocimetry based on image and object space information. ISPRS Commission V Symposium, Corfu, Greece, September 2–6, 2002.
Willneff, J., Wenisch, O., 2011. The calibration of wide angle lens cameras using perspective and non-perspective projections in the context of real-time tracking applications. Videometrics, Range Imaging, and Applications Xi, 8085.